ARTICLES
PUBLISHED ONLINE: 19 OCTOBER 2015 | DOI: 10.1038/NPHOTON.2015.198
nature photonics

On-chip zero-index metamaterials

Yang Li[1†], Shota Kita[1†], Philip Muñoz[1], Orad Reshef[1], Daryl I. Vulis[1], Mei Yin[1,2], Marko Lončar[1*] and Eric Mazur[1,3*]

Metamaterials with a refractive index of zero exhibit physical properties such as infinite phase velocity and wavelength. However, there is no way to implement these materials on a photonic chip, restricting the investigation and application of zero-index phenomena to simple shapes and small scales. We designed and fabricated an on-chip integrated metamaterial with a refractive index of zero in the optical regime. Light refracts perpendicular to the facets of a prism made of this metamaterial, directly demonstrating that the index of refraction is zero. The metamaterial consists of low-aspect-ratio silicon pillar arrays embedded in a polymer matrix and clad by gold films. This structure can be fabricated using standard planar processes over a large area in arbitrary shapes and can efficiently couple to photonic integrated circuits and other optical elements. This novel on-chip metamaterial platform opens the door to exploring the physics of zero index and its applications in integrated optics.

Metamaterials—composite materials whose electromagnetic properties are engineered by structuring their constituents[1,2]—make it possible to achieve a refractive index equal to zero[3]. When the index of refraction is zero, the phase velocity is infinite. In this extreme limit, the wavelength inside the material is infinite and the phase is uniform throughout, regardless of its overall size and shape. All fields within the material oscillate in unison, achieving electrostatic behaviour at optical frequencies[4]. This regime allows access to a wealth of exciting physical phenomena and potential applications, including super-coupling, cloaking and new approaches for phase matching in nonlinear optics[3,5–9].

Experimental demonstrations of zero-index metamaterials typically involve metals operating around their plasma frequencies[10–12], or metallic resonators[13–16], resulting in high loss and impedance mismatch. Recently, zero index was demonstrated by tuning the Mie resonances in a purely dielectric photonic crystal structure[17,18]. This approach offers several important advantages. First, dielectric metamaterials avoid the losses associated with metals, especially in the optical regime. Second, tuning the Mie resonances allows for the simultaneous control of the electric and magnetic response[19,20]. In particular, when the effective relative permittivity $\varepsilon_r^{\mathrm{eff}}$ and permeability μ_r^{eff} approach zero simultaneously, the impedance $\eta_{\mathrm{eff}} = \sqrt{\mu_r^{\mathrm{eff}}/\varepsilon_r^{\mathrm{eff}}}$ can be matched to that of other materials.

For integrated photonic applications, zero-index metamaterials require light to be confined on-chip and thus need to be realized in an in-plane geometry (that is, with the light propagating parallel to the substrate). This geometry would permit these metamaterials to be integrated with other optical elements, including waveguides, resonators and interferometers. To date, zero-index metamaterials have been demonstrated only in an out-of-plane geometry, with functional layers of the metamaterials stacked on a substrate and where light propagates normal to the sample surface[12,16,18]. This geometry is not only impractical for integrated-photonics applications, but is also limited to short interaction lengths and cannot be fabricated in arbitrary shapes.

In this Article, we present an on-chip, in-plane metamaterial with zero index in the telecom wavelength range. Our design consists of a square array of low-aspect-ratio silicon pillars on a silicon-on-insulator (SOI) substrate. The array is embedded in an SU-8 slab waveguide and clad above and below by gold films. This metamaterial was fabricated using conventional nanofabrication processes (Fig. 1a). First, we define an array of pillars in a 512-nm-thick silicon device layer using electron-beam lithography followed by inductively coupled plasma reactive ion etching (step I in Fig. 1a). Next, we use electron-beam evaporation to deposit a 50-nm-thick gold film (step II). We then embed the pillars within a 595-nm-thick SU-8 photoresist layer (step III). Finally, a second gold film is deposited to complete the fabrication process (step IV). We can produce arbitrarily shaped pillar arrays using such conventional planar fabrication techniques to realize a variety of metamaterial devices.

We demonstrate zero index by measuring the refraction through a prism made of this metamaterial (Fig. 1b) with a 1.5-μm-thick SU-8 matrix (see last paragraph of next section and Supplementary Section 1). A silicon waveguide oriented perpendicular to one of the prism facets guides the incident beam (Fig. 1b). Light that enters the prism is refracted at the output facet into a semi-circular slab of SU-8, which we use to determine the angle of refraction (Fig. 1b,c). The measured angles of refraction are in excellent agreement with simulations and unambiguously demonstrate that the metamaterial prism has zero index at a wavelength of 1,570 nm.

Design

Previous designs for dielectric zero-index metamaterials have been based on infinitely long silicon pillars[17,18]. These designs are incompatible with integrated silicon photonic platforms, which are typically based on silicon device layers with thickness on the order of the wavelength. One can replicate the behaviour of infinitely long pillars by placing short silicon pillars between parallel conductors[21]. This approach reduces the out-of-plane radiation loss and enforces the fundamental transverse magnetic (TM) mode by ensuring that the electric field between the parallel conductors is along the pillar axis (Supplementary Section 2). Accordingly, it preserves the impedance-matched zero index using a structure of finite

[1]School of Engineering and Applied Sciences, Harvard University, 9 Oxford Street, Cambridge, Massachusetts 02138, USA. [2]State Key Laboratory of Advanced Optical Communication Systems and Networks, School of Electronics Engineering and Computer Science, Peking University, 5 Yiheyuan Road, Beijing 100871, China. [3]Department of Physics, Harvard University, 9 Oxford Street, Cambridge, Massachusetts 02138, USA. †These authors contributed equally to this work. *e-mail: loncar@seas.harvard.edu; mazur@seas.harvard.edu

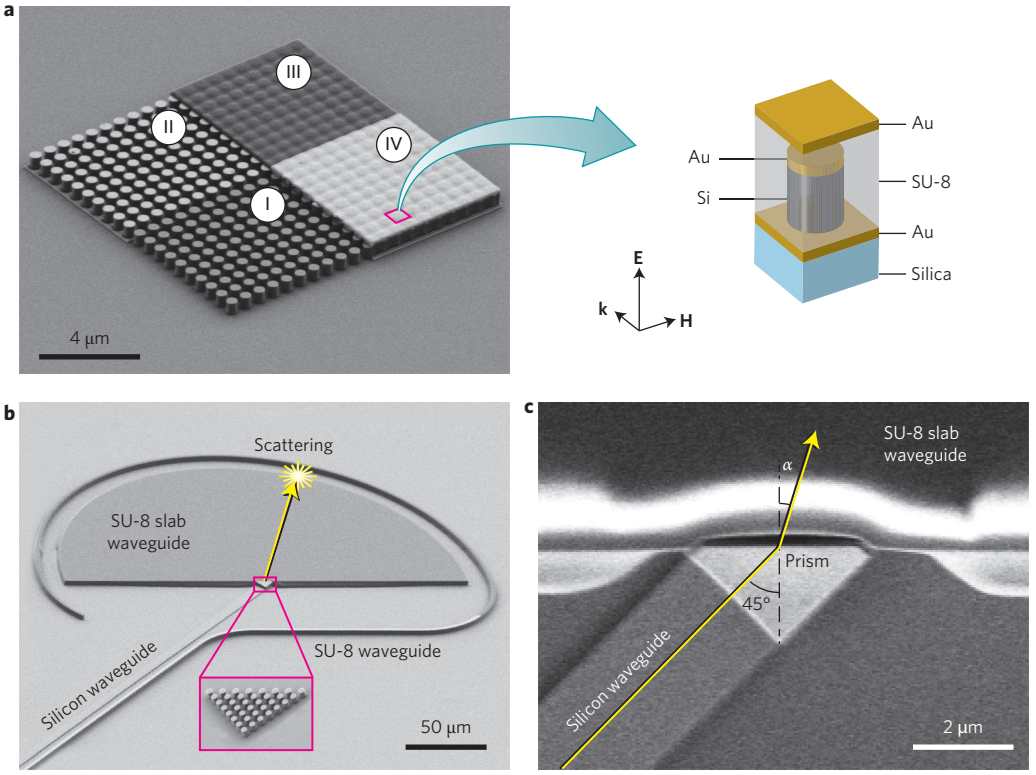

Figure 1 | Metamaterial design and structure fabricated to demonstrate in-plane zero index. a, Scanning electron microscopy image of the metamaterial at different fabrication stages: I, silicon pillars etched from SOI substrate; II, with bottom gold film; III, embedded in SU-8 matrix; IV, completed structure with top gold film. Inset: three-dimensional schematic of one unit cell of the metamaterial. The pitch and radius of the silicon pillars are 690 nm and 211 nm, respectively. **b**, A silicon waveguide carries the incident beam towards the metamaterial prism, where the beam is refracted into the SU-8 slab waveguide. Inset: the prism, which is a right triangular array of pillars measuring eight unit cells across, without gold and SU-8 layers. **c**, Prism region showing the incident and refracted beams. The angle of refraction α is determined by measuring the position of the refracted beam at the curved output edge of SU-8 slab waveguide (yellow scattering spot in **b**).

height and allows the metamaterial to be integrated with conventional nanophotonic components (Fig. 1). The pitch and radius of the silicon pillar array are adjusted to obtain zero index with low propagation loss at a wavelength of 1,590 nm, near the middle of the 1,480–1,680 nm tuning range of our laser (Supplementary Section 3). Propagation loss in this metamaterial is dominated by the conduction loss originating from the gold films (Supplementary Section 4).

To characterize the optical properties of the designed metamaterial, we calculated its band structure in the plane of the array (Fig. 2a). As Fig. 2a shows, two linear dispersion bands intersect at the Γ point. These bands form a Dirac-like cone (blue, Fig. 2b) intersecting a quadratic dispersion band (red) at the Dirac point at the centre of the Brillouin zone[17]. The two linear-dispersion bands correspond to electric monopole and transverse magnetic dipole modes near the Dirac point (Fig. 2c). At the Dirac point, the wavenumber approaches zero, indicating that the effective index of the metamaterial is also zero. Furthermore, the nearly circular isofrequency contours in a 55 nm bandwidth around the Dirac point (Fig. 2d) suggest that the metamaterial is essentially isotropic, producing a refractive index of zero in almost all propagation directions. The effective wavelength λ_{eff} approaches infinity in the vicinity of the Γ point, satisfying the homogenization criterion[17,18,22] and allowing us to treat the metamaterial as a homogeneous bulk medium with effective constitutive parameters in the vicinity of the Dirac point (Supplementary Section 5). We can retrieve the effective relative permittivity $\varepsilon_{\mathrm{r}}^{\mathrm{eff}}$ and permeability $\mu_{\mathrm{r}}^{\mathrm{eff}}$ of this metamaterial from the simulated reflection and transmission coefficients (Fig. 2e)[23]. The computed $\varepsilon_{\mathrm{r}}^{\mathrm{eff}}$ and $\mu_{\mathrm{r}}^{\mathrm{eff}}$ cross zero simultaneously and linearly at the design wavelength of 1,590 nm, with an effective impedance of 1.47. This simultaneous and linear electric and magnetic response is a unique characteristic of zero-index metamaterials corresponding to Dirac cones, and is essential to achieve a finite impedance[17]. The $\varepsilon_{\mathrm{r}}^{\mathrm{eff}}$ and $\mu_{\mathrm{r}}^{\mathrm{eff}}$ are only linear in the vicinity of the Dirac-point wavelength[17]. All these results indicate that this metamaterial possesses a relatively isotropic zero effective index with good impedance matching to free space and to standard optical waveguides.

Our simulations show that a Dirac cone can be obtained even for significantly larger SU-8 layer thicknesses (Supplementary Section 6), providing more flexibility in the fabrication process. Because it is difficult to spin on a very thin SU-8 layer between the silicon pillars right next to a large tapered waveguide, we chose to use a 1.5-μm-thick, rather than a 595-nm-thick SU-8 layer in the fabrication of our prisms (Fig. 1b,c).

Experimental results

To experimentally measure the refractive index of the metamaterial, we illuminated the metamaterial prism and measured the angle of the refracted beam (Fig. 1b,c). The prism was illuminated with TM-polarized light delivered via the tapered silicon waveguide. The light propagates through the prism with an effective index n_1^{eff} and reaches the interface between the prism and the SU-8 slab waveguide at an angle of incidence of 45°. The refracted beam then propagates as a guided mode of the SU-8 slab waveguide with known effective index n_2^{eff}, until it is scattered at the semicircular edge of the SU-8 slab waveguide (Supplementary Section 7). The scattered light was imaged from above using an infrared camera to

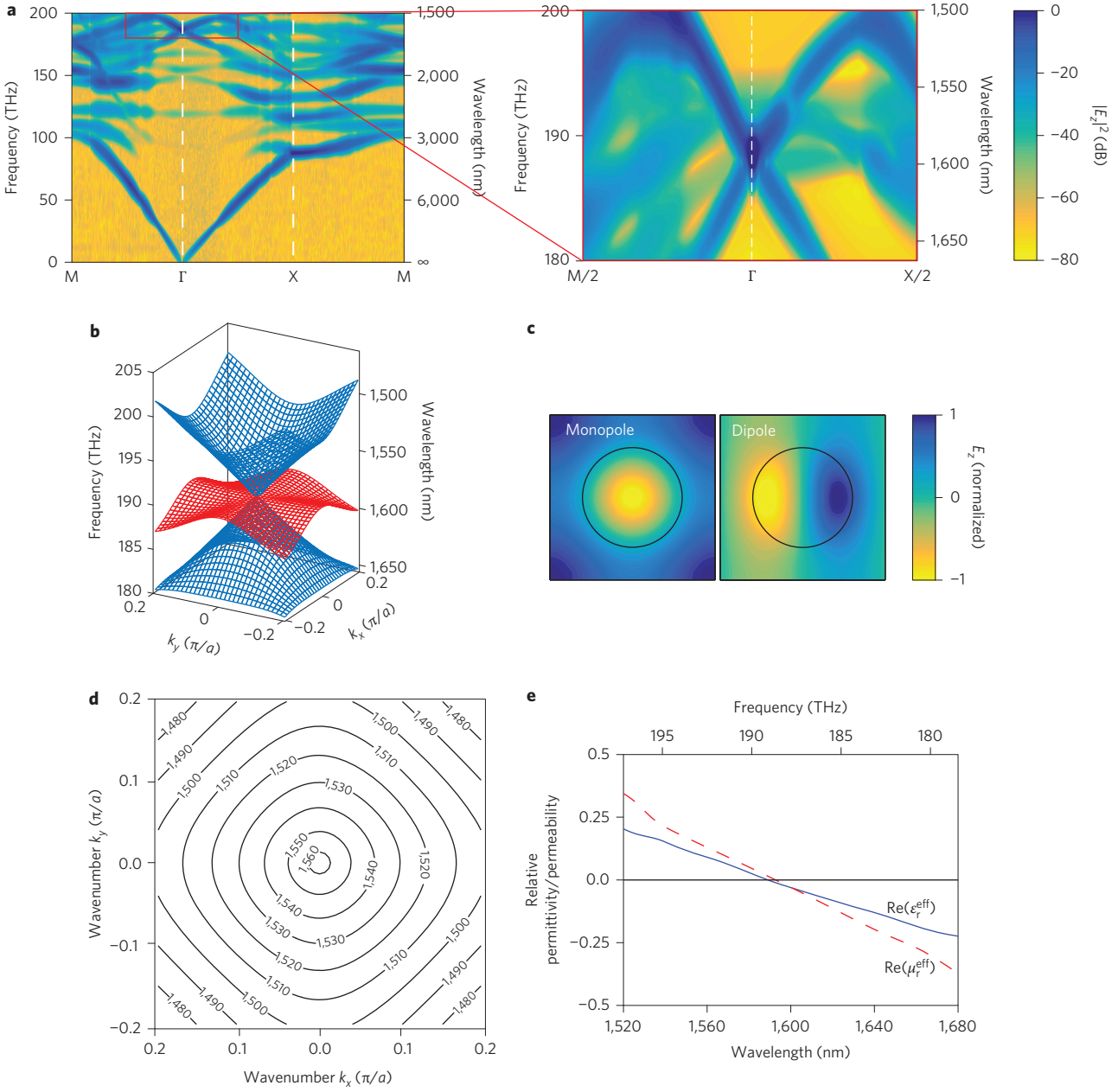

Figure 2 | Optical properties of the zero-index metamaterial. a, Photonic band structure of the zero-index metamaterial (Fig. 1a) for TM modes. Two linear dispersion bands intersect at the Γ point at $\lambda = 1{,}590$ nm. **b**, Three-dimensional dispersion surfaces. The linear bands (blue) form a Dirac-like cone. The quadratic band (red) is a quasi-longitudinal mode[17]. We show only the three modes that form the cone to emphasize the Dirac-cone dispersion clearly. **c**, Electric fields at the Dirac point over a unit-cell cross-section in the plane of the array, corresponding to an electric monopole mode and a transverse magnetic dipole mode. Black circles indicate the boundary of the silicon pillar. **d**, Isofrequency contours of the zero-index metamaterial. The nearly circular contours indicate that this metamaterial is almost isotropic near the Γ point. **e**, Effective relative permittivity (blue line) and permeability (red dashed line) of the metamaterial retrieved from simulated reflection and transmission coefficients. Both parameters cross zero simultaneously, resulting in finite impedance.

determine the refraction angle α. This refraction angle was used to determine n_1^{eff} using Snell's law: $n_2^{\mathrm{eff}}/n_1^{\mathrm{eff}} = \sin 45^\circ/\sin\alpha$.

Figure 3a shows the experimentally observed refraction in the prism and the SU-8 slab waveguide at $\lambda = 1{,}570$ nm, where the metamaterial shows zero index (Supplementary Section 8). Because of fabrication imperfections, this wavelength is slightly different from the design wavelength of 1,590 nm. The yellow arrow in Fig. 3a shows the refracted beam, which propagates perpendicular to the interface between the prism and SU-8 slab waveguide, corresponding to a prism with a refractive index of zero. The prism also generates several side beams at $\lambda = 1{,}570$ nm due to additional modes in the band structure (Fig. 2a, Supplementary Section 9).

Figure 3b shows the corresponding numerical calculation of the out-of-plane electromagnetic field distribution in the prism and the SU-8 slab waveguide region at $\lambda = 1{,}570$ nm. As in the observed results, the refracted beam propagates perpendicular to the interface between the prism and SU-8 slab waveguide, with several side beams appearing on either side. As shown in the magnified view on the right in Fig. 3b, there is no spatial phase variation within the prism, as the effective wavelength is infinite inside the metamaterial.

We probed the dispersion of the metamaterial index by measuring the angle of refraction while varying the input wavelength from 1,480 to 1,680 nm. The left panel of Fig. 3c shows the intensity measured along the curved output edge of the SU-8 slab waveguide

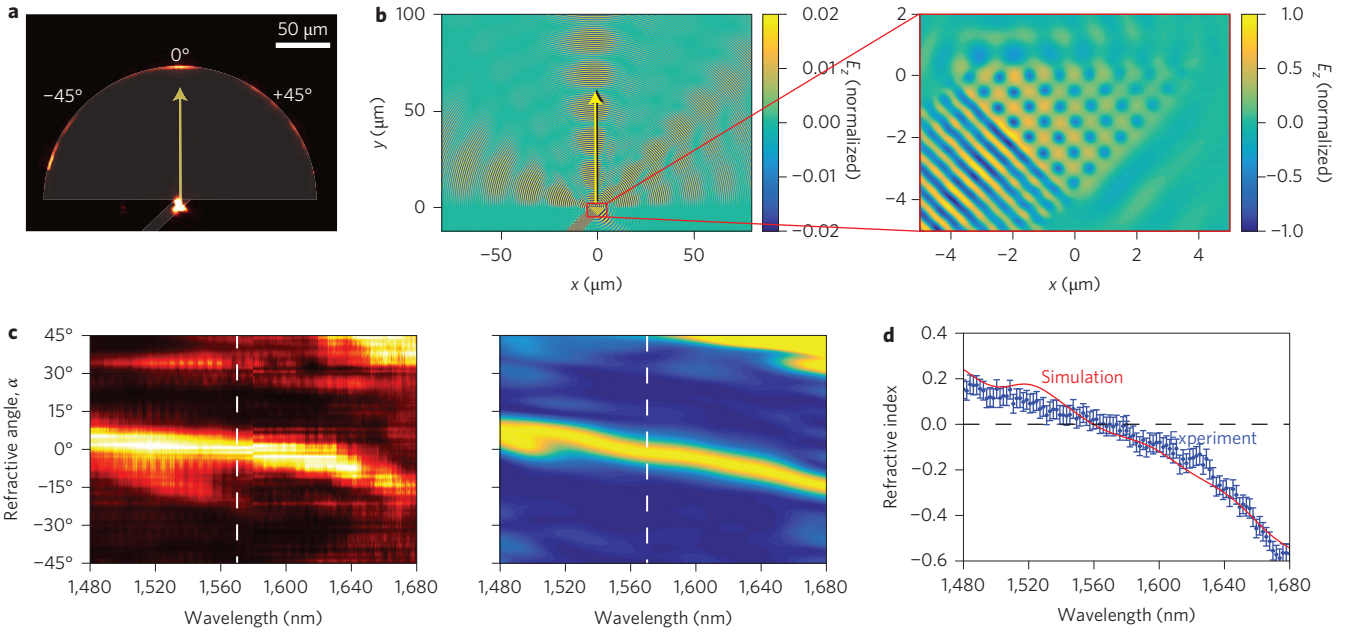

Figure 3 | Simulation and experimental results. a, Near-infrared microscope image of the prism (Fig. 1b,c) at 1,570 nm, showing the refracted beam, which propagates normal to the interface between the prism and the SU-8 slab waveguide. The grey area corresponds to the silicon waveguide and SU-8 slab waveguide. **b**, Left: simulated out-of-plane electric field ($\lambda = 1{,}570$ nm) in the prism and SU-8 slab waveguide region. The refracted beam is visible at the curved output edge of the SU-8 slab waveguide at 0°. Right: magnified view of the electric field distribution in the prism, illustrating the nearly constant spatial phase distribution. **c**, Measured (left) and simulated (right) far-field patterns. The white dashed line indicates the wavelength, 1,570 nm, at which the refracted beam crosses 0°. The image is normalized at each wavelength. **d**, Measured and simulated effective index of the zero-index metamaterial. Blue dots indicate the measured refractive index, and error bars represent uncertainties in the measurement.

as a function of wavelength and refraction angle. The right panel of Fig. 3c shows the corresponding simulated far-field pattern (Supplementary Section 10). We observe excellent agreement between the measured and simulated far-field patterns, with both patterns showing the refracted beam in the centre, near 0°. The shifting of the refracted beam indicates that the refractive index of the prism continuously changes from a positive value at shorter wavelengths to a negative value at longer wavelengths.

Using Snell's law, we extract the index of refraction of the metamaterial from the position of the refracted beam in the wavelength range 1,480–1,680 nm (Supplementary Section 11). As shown in Fig. 3d, the measured index varies from 0.15 ± 0.04 at 1,480 nm to -0.57 ± 0.04 at 1,680 nm, exhibiting linear dispersion near the zero crossing at 1,570 nm. The error bars represent uncertainties in the measured index due to finite image resolution and fitting uncertainty (Supplementary Section 11). Using a similar extraction method, we calculated the index of refraction from the simulated far-field patterns, showing excellent agreement with measured values.

To determine whether our measured zero index is caused by a Dirac cone or by a small bandgap, we measured two prisms with both smaller and larger pillar radii. Theoretically, a photonic Dirac cone has no bandgap at the Dirac-point wavelength. Due to fabrication imperfections, however, a tiny bandgap may open near the targeted Dirac-point wavelength of the fabricated zero-index metamaterial. In that case, the real part of the index has a constant zero value rather than linear dispersion. Given our error bars (Fig. 3d), the bandgap is at most 50 nm wide. Index measurements of prisms with smaller or larger radii show that the bandgaps of these metamaterials are blueshifted or redshifted, respectively. In addition, the bandgaps of those with larger radii become significantly wider. This behaviour confirms that the experimentally measured zero index in Fig. 3 corresponds to a Dirac cone at the Γ point[17] (Supplementary Section 12).

As a control, we also measured the refractive index in the absence of the metamaterial prism. In this control experiment, light from the input silicon waveguide propagates through free space before refracting into the SU-8 slab waveguide. The measured index of the void is 0.94 ± 0.04 in the wavelength range 1,480–1,680 nm, in good agreement with the index of air (Supplementary Section 13). Therefore, the measured index shown in Fig. 3 corresponds to the effective index of the metamaterial prism, rather than being an artefact of the measurement set-up.

Conclusion

We have experimentally demonstrated the first on-chip integrated zero-index metamaterial in the optical regime and directly measured the effective index of a prism consisting of this material. The metamaterial is effectively two-dimensional, as energy propagates in the plane of the array. This in-plane structure can efficiently couple to silicon waveguides to interface with standard integrated photonic components. Using standard planar processes, the metamaterial can be fabricated over a large area with high fidelity and in arbitrary shapes. This design enables direct implementation of zero-index phenomena on a chip, including super-couplers, surface-emitting lasers and new approaches for phase-matching in nonlinear optics[3,5,8,9,24]. It can also serve as an on-chip lab to explore fundamental quantum science such as photon entanglement and enhancement of spontaneous emission[4,18].

Methods

Methods and any associated references are available in the online version of the paper.

Received 1 April 2015; accepted 17 September 2015;
published online 19 October 2015

References

1. Soukoulis, C. M. & Wegener, M. Past achievements and future challenges in the development of three-dimensional photonic metamaterials. *Nature Photon.* **5,** 523–530 (2011).

2. Engheta, N. & Ziolkowski, R. W. *Metamaterials: Physics and Engineering Explorations* (Wiley, 2006).
3. Engheta, N. Pursuing near-zero response. *Science* **340,** 286–287 (2013).
4. Mahmoud, A. M. & Engheta, N. Wave–matter interactions in epsilon-and-mu-near-zero structures. *Nature Commun.* **5,** 5638 (2014).
5. Silveirinha, M. & Engheta, N. Tunneling of electromagnetic energy through subwavelength channels and bends using ε-near-zero materials. *Phys. Rev. Lett.* **97,** 157403 (2006).
6. Hao, J. M., Yan, W. & Qiu, M. Super-reflection and cloaking based on zero index metamaterial. *Appl. Phys. Lett.* **96,** 101109 (2010).
7. Nguyen, V. C., Chen, L. & Klaus, H. Total transmission and total reflection by zero index metamaterials with defects. *Phys. Rev. Lett.* **105,** 233908 (2010).
8. Rose, A. & Smith, D. R. Overcoming phase mismatch in nonlinear metamaterials. *Opt. Mater. Express* **1,** 1232–1243 (2011).
9. Suchowski, H. *et al.* Phase mismatch-free nonlinear propagation in optical zero-index materials. *Science* **342,** 1223–1226 (2013).
10. Pendry, J. B., Holden, A. J., Stewart, W. J. & Youngs, I. Extremely low frequency plasmons in metallic mesostructures. *Phys. Rev. Lett.* **76,** 4773–4776 (1996).
11. Boltasseva, A. & Atwater, H. A. Low-loss plasmonic metamaterials. *Science* **331,** 290–291 (2011).
12. Maas, R., Parsons, J., Engheta, N. & Polman, A. Experimental realization of an epsilon-near-zero metamaterial at visible wavelengths. *Nature Photon.* **7,** 907–912 (2013).
13. Pendry, J. B., Holden, A. J., Robbins, D. J. & Stewart, W. J. Magnetism from conductors and enhanced nonlinear phenomena. *IEEE Trans. Microw. Theory Tech.* **47,** 2075–2084 (1999).
14. Shelby, R. A., Smith, D. R. & Schultz, S. Experimental verification of a negative index of refraction. *Science* **292,** 77–79 (2001).
15. Liu, R. *et al.* Experimental demonstration of electromagnetic tunneling through an epsilon-near-zero metamaterial at microwave frequencies. *Phys. Rev. Lett.* **100,** 023903 (2008).
16. Valentine, J. *et al.* Three-dimensional optical metamaterial with a negative refractive index. *Nature* **455,** 376–379 (2008).
17. Huang, X. Q., Lai, Y., Hang, Z. H., Zheng, H. H. & Chan, C. T. Dirac cones induced by accidental degeneracy in photonic crystals and zero-refractive-index materials. *Nature Mater.* **10,** 582–586 (2011).
18. Moitra, P. *et al.* Realization of an all-dielectric zero-index optical metamaterial. *Nature Photon.* **7,** 791–795 (2013).
19. Staude, I. *et al.* Tailoring directional scattering through magnetic and electric resonances in subwavelength silicon nanodisks. *ACS Nano* **7,** 7824–7832 (2013).
20. Evlyukhin, A. B. *et al.* Optical spectroscopy of single Si nanocylinders with magnetic and electric resonances. *Sci. Rep.* **4,** 4126 (2014).
21. Balanis, C. A. *Engineering Electromagnetics* (Wiley, 1989).
22. Simovski, C. R. On electromagnetic characterization and homogenization of nanostructured metamaterials. *J. Opt.* **13,** 013001 (2011).
23. Smith, D. R., Vier, D. C., Koschny, T. & Soukoulis, C. M. Electromagnetic parameter retrieval from inhomogeneous metamaterials. *Phys. Rev. E* **71,** 036617 (2005).
24. Chua, S.-L., Lu, L., Bravo-Abad, J., Joannopoulos, J. D. & Soljačić, M. Larger-area single-mode photonic crystal surface-emitting lasers enabled by an accidental Dirac point. *Opt. Lett.* **39,** 2072–2075(2014).

Acknowledgements

The authors thank X.Q. Huang, Y. Wu, C. Simovski, C.C. Evans and Y.M. Yang for discussions, N. Liu for assistance with finite-difference time-domain simulations, Q.M. Quan for assistance with the measurements, M. Kats for providing the measured complex index of gold and K. Phillips for guidance on the preparation of the figures. The research described in this Article was supported by the National Science Foundation under contract DMR-1360889, the Air Force Office of Scientific Research under contract FA9550-14-1-0389, the Natural Sciences and Engineering Research Council of Canada and the Harvard Quantum Optics Center.

Author contributions

Y.L. conceived the basic idea for this work. Y.L., P.M. and D.V. carried out the FDTD simulations. S.K., O.R. and M.Y. carried out the FEM simulations. O.R. designed the optical waveguides. S.K. performed the fabrication. S.K., O.R. and D.V. carried out the measurements. P.M. analysed the experimental results. M.L. and E.M. supervised the research and the development of the manuscript. Y.L. wrote the first draft of the manuscript, and all authors subsequently took part in the revision process and approved the final copy of the manuscript.

Additional information

Supplementary information is available in the online version of the paper. Reprints and permissions information is available online at www.nature.com/reprints. Correspondence and requests for materials should be addressed to M.L. and E.M.

Competing financial interests

The authors declare no competing financial interests.

Methods

Simulations. The complex indices of gold, silicon and silica for use in numerical simulations were measured using spectroscopic ellipsometry. The complex reflection and transmission coefficients, electromagnetic field profiles and far-field patterns were calculated using three-dimensional finite-difference time-domain simulations. Reflected and transmitted electric fields were extracted at one point before the source and one after the metamaterial, respectively, to obtain the complex reflection and transmission coefficients (Supplementary Fig. 26). The electric fields were collected from a near-field simulation to obtain the far-field pattern using far-field projection.

The band structures, dispersion surfaces and isofrequency contours were computed using three-dimensional finite element method simulations. These results were obtained by first calculating all the modes in a unit cell of the metamaterial with Floquet periodic boundary conditions in the x and y directions and perfectly matched layers at the boundaries in the z direction. TM-polarized modes were selected by evaluating the energy ratio of the electric fields in the x, y and z directions. Modes with low quality factors (<10) or low core confinements in the metamaterial region were filtered out.

Fabrication. The zero-index metamaterial was fabricated on a SOI wafer using standard lithographic techniques (Fig. 1). Beginning with a 512-nm-thick silicon layer, the silicon pillars and coupling waveguides were patterned into negative-tone resist (XR-1541 6%, Dow Corning) using electron-beam lithography (EBL) and were subsequently structured using inductively coupled plasma reactive ion etching (ICP-RIE). A layer of positive-tone resist (PMMA 495 C6, MicroChem) was spin-coated and patterned using EBL, designating the location of the bottom gold film. A 5-nm-thick titanium adhesion layer and a 95-nm-thick gold layer were deposited using electron-beam evaporation and were subsequently lifted off by acetone boiling and very weak sonication to serve as the bottom gold film. Following this step, a 1.5-μm-thick SU-8 layer was spin-coated then cured using EBL, to form the polymer matrix around the silicon pillars to support the top gold film. The steps to structure and deposit the top gold film were the same as those for the bottom gold film.

To fabricate the four-part cut-away showing each fabrication step (Fig. 1a), we masked each quadrant individually using a positive tone resist before following the fabrication procedure outlined above.